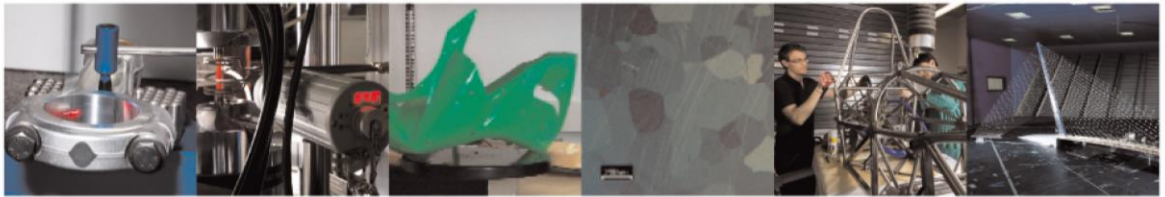DIPARTIMENTO DI MECCANICA

mecc

A novel paradigm for feedback control in LPBF: layer-wise correction for overhang structures

Vasileska E.; Demir A.G.; Colosimo B.M.; Previtali B.

A novel paradigm for feedback control in LPBF: layer-wise correction for overhang structures

Ema Vasileska[1,*], Ali Gökhan Demir[1], Bianca Maria Colosimo[1], Barbara Previtali[1]

[1]Department of Mechanical Engineering, Politecnico di Milano, Via La Masa 1, 20156 Milan, Italy

*Corresponding author, ema.vasileska@polimi.it

A novel paradigm for feedback control in LPBF: layer-wise correction for overhang structures

Abstract

In laser powder bed fusion (LPBF), it is common practice to select process parameters to achieve high density parts starting from simple geometries such as cubes or cylinders. However, additive manufacturing (AM) is usually adopted to produce very complex geometries, where parameters should be tuned locally, depending on the local features to be processed. In fact, geometrical features, such as overhangs, acute corners, and thin walls may lead to over- or under-heating conditions, which may result in geometrical inaccuracy, high roughness, volumetric errors (i.e., porosity) or even job failure due to surface collapse. This work proposes a layer-wise control strategy to improve the geometrical precision of overhanging regions using a coaxial melt pool monitoring system. The melt-pool images acquired at each layer are used in a control-loop to adapt the process parameters locally at the next layer in order to minimize surface defects. In particular, the laser duty cycle is used as a controllable parameter to correct the energy density. This work presents the main architecture of the proposed approach, the control strategy and the experimental procedure that need to be applied to design the control parameters. The layer-wise control strategy was tested on AISI 316L stainless steel using an open LPFB platform. The results showed that the proposed layer-wise control solution results in a constant melt pool observed via the laser heated area size starting from the second layer onward, leading to a significant improvement in the geometrical accuracy of 5 mm-long bridge geometries.

Keywords: Closed-loop control, melt pool monitoring, defect correction, pulsed-wave emission.

1 Introduction

Laser powder bed fusion (LPBF) is arguably the most mature industrial additive manufacturing process for producing metal components. However, the process still requires further development as the demand for single to small lots of high value products increase. A production scheme of this type requires LPBF that is able to produce defect-free components that vary in size and dimensions correctly the first time. The need for monitoring and online control solutions increase accordingly [1]. The shape and size variability of the components render the LPBF process vulnerable to the formation of defects, despite the use of optimized process parameters.

Online and in-situ process monitoring aims to detect the onset of defects by modelling and monitoring in-situ data (images, video and signals) [2]. Several approaches can be employed to gather data on the process dynamics. Optical, mechanical, and acoustic methods commonly gather indirect process magnitudes such as temperature measurements [3], photonic radiation [4], and airborne and mechanical vibrations [5]. Amongst the indirect approaches, melt pool geometry measurement is an appealing approach to link the thermal behaviour of the process to part quality [6]. In this case, it is assumed that the right selection of process parameters has already been carried out but statistical data monitoring of real-time data (e.g., images, spatters or cooling profiles) is needed to quickly detect unnatural and unexpected process changes. Once the defect is detected, the process can be stopped simply, while the newly developed hybrid additive/subtractive systems can allow for defect removal [7]. Concerning the direct approaches, several examples of measurement devices integrated into powder bed fusion machines have been demonstrated, such as measuring the part's geometry via powder bed imaging [8], the surface roughness by low-coherence interferometry measurements [9] or the investigation of the material's microstructure by spatially resolved acoustic spectroscopy [10], and formation of porosity by X-ray imaging [11]. Although direct approaches

provide straightforward measurements of the defects formed, their integration into existing systems can be difficult and invasive due to the size, cost, and safety requirements. In most cases, the data generated can be excessive for an inline evaluation and control scheme. Moreover, the capability of capturing the defect formation cue through the use of an indirect method, such as thermal imaging, was demonstrated by comparison with the direct measurements using X-ray imaging [12].

Commonly, the process parameters utilized on a LPBF machine are optimised for a certain material in order to obtain sufficient part density without compromising productivity. Often simple geometries such as cubes or cylinders are used for studying the process parameters. Once the process parameters are chosen, they are expected to be used throughout the entire production of the system. This approach neglects parameter variations required to compensate for the geometrical variety employed in the process. Indeed, the local geometry surrounding the laser-material interaction zone can largely influence the locally concentrated temperature gradient and hence the melt pool size. The use of static process parameters determined *a-priori* does not consider the part's geometry or any potential in-process defects, leading to an increase in the melt pool size. As a consequence of the increase in size of the melt pool due to excessive energy, porosity, thermal deformation, cracking, increase of surface roughness, and swelling may occur [13]. To counterbalance the redundancy of employing a fixed set of process parameters several design rules are employed. For instance, overhang regions longer than 1 mm, and bridged gaps larger than 3 mm should be supported [14]. Support structures are also recommended for thin sections and pointy edges to avoid heat accumulation. While the use of support structures can be an effective solution, their removal and post processing stages are time consuming and add further expense on terms of production.

On the other hand, the melt pool size might be controlled by managing the energy release on the material [15]. One of the ways to effectively control the energy release and consequently the melt pool size is by changing the laser emission profile [16]. It was shown that pulsed wave (PW) emission by laser power modulation can be beneficial for producing thin structures [17], while continuous wave (CW) emission is preferable for maintaining high density in large components [18]. Recently, the complementary use of CW and PW emission on large and thin regions respectively was shown to be effective for maintaining a stable melt pool within the processed part [19]. However, in real industrial applications, part geometries as well as scanned layer shape vary much more greatly than those presented in literature. Moreover, such variations can coincide with other heat accumulation causes, different from large or thin area, such as regions overhanging on a power bed. Therefore, *a-priori* setting of process parameters as well as *a-priori* knowledge of part variations inside the layer cannot be sufficient to prevent the onset of defects due to melt pool instability. Thus, development of feedback control strategies is critically important in order to overcome geometrical variations. Having an insight into the melting conditions in the earliest stage of the building process can reduce the possibility of defects forming by enabling corrective actions on the process parameters. In this way process parameters can be adapted to the part's geometry in real-time.

In literature, real-time control systems have been employed in laser-based manufacturing processes, such as laser welding, cutting and cladding. Hofman et al. [20] developed a camera-based control system on a laser cladding platform using identification experiments and control theory, which adjusts the laser power in real-time to compensate for the heat accumulation so that the width of the melt pool remains at a reference value. Song et al. [21] measured the melt pool temperature in the laser cladding process using a dual-colour pyrometer. They identified the melt pool temperature dynamics related to the laser power and implemented a predictive control algorithm to maintain it at a steady-state value. There have been several works regarding control in laser cutting and welding, which implement on-axial and off-axial camera modules, as well as photodiodes, to monitor the thermal or plasma emission of the process and adjust the cutting process parameters based on the sensor's output

[22], [23]. While they provide insights for controlling the LPBF process, all these processes have a common factor in that they involve less strict conditions concerning the temporal and spatial acquisition conditions. This is one of the critical points limiting the development of real-time closed-loop control strategies for LPBF.

Due to the limitations related to the real-time control of process parameters in LPBF, different methods have been developed in literature for evaluating the process and optimizing the parameters. Additional processing strategies concerning defect formation such as the use of pre-heating of the powder bed [24] and re-melting the last scanned layer [25] were demonstrated. For *a-priori* analysis of the process parameters, offline simulations based on Finite Element Methods and Machine Learning techniques can provide the possibility of simulating the process and predicting or adjusting the parameters in order to achieve desired mechanical properties [26]. Lately, the simulation tools have also reached industrial maturity providing sufficiently accurate results with reasonable calculation times. Although offline solutions based on process simulations are becoming faster [27], they rely highly on metamodels involving a larger number of experiments. Most of the commercial software packages concentrate on macro-geometrical defects resulting from thermal distortions. A possible solution is using geometrical compensation of the part's model. Their applicability to process parameters and scan strategy variations are also limited [28]. Recently, feedforward control schemes through the use of thermal simulations were also proposed [29]. The use of analytical models with fast solutions to feedforward the process parameters were found to be successful at a single layer level, proving to be highly promising for further implementation. On the other hand, the use of closed-loop control systems remains highly desirable both as an alternative and as a complementary solution.

Despite these challenges related to the temporal and spatial limitations, some pioneering work has been carried out in literature concerning the closed-loop control of LPBF. An effective way of assessing process performance and quality is by coaxial monitoring of the optical radiation emitted by the process area around the laser spot, specifically monitoring the near infrared radiation of the melt pool [30]. Among the melt pool feedback controllers found in literature, most target the melt pool area. Renken et al. [31] employed real-time control of the laser power reliant on a pyrometer signal, by designing and employing a cascade proportional (P) controller. A reduction of process temperature deviation was achieved which led to more stable conditions in the melt pool. Yeung et al. [32] presented a jerk-limited motion control for improving position and velocity accuracy, considering the output signal of a high-speed coaxial camera implemented on a LPBF platform. Several research activities related to closed-loop control in LPBF have been conducted by KU Leuven [33], [34], where P and proportional–integral (PI) controllers were developed by implementing a coaxial photodiode and CMOS camera and controlling the laser power based on the pyrometer's signal. By modulating the laser power with a multi sine function, Craeghs et al. [33] identified that the dynamic relation between the laser power and the photodiode signal is adequately fitted with a second order model. Overhanging structures were effectively built with improved properties and the potentiality of adapting the scanning parameters in LPBF was concluded. Despite the pioneering nature of these works, one of the issues was related to the fact that the processing speeds were slower (approximately 80 mm/s scan speed) compared to what is applied today (400-1500 mm/s), which require faster acquisition rates. To the authors' knowledge, no previous work has managed to achieve closed-loop control in real time at the conventional processing speeds of LPBF with the use of a camera as a feedback sensor. On the other hand, industrial LPBF system manufacturers started to implement coaxial monitoring systems for monitoring the melt pool. However, effective control strategies exploiting these sensors are not yet fully developed. This is due to the time required to evaluate the required data to implement a control action and the missing control strategies. As indicated by Hirsch et al, between successive layers of a powder bed fusion process, the time required for recoating can be used to complete the analysis of the monitoring data [35]. This opens the possibility of a control strategy that should

4

correct defect formation and stop its propagation. However, effective control strategies have not yet been developed for a layer-wise approach of this kind.

Therefore, this work aims to investigate a closed-loop control strategy for producing large overhang regions by adapting the process parameters in a layer-wise control scheme close to the industrial production conditions. The near infrared (NIR) images of the melt pool were acquired with a coaxial monitoring system and evaluated for each layer. Conditions with overheating, hence, with excessively large melt pool indicated by the laser heated area measurements were corrected by lowering the duty cycle, thus moving towards the PW emission. With this concept, the duty cycle of each scan vector was corrected for the successive layer.

This work is organized as follows. Initially the open LPBF platform with coaxial monitoring capability and the control strategy are presented. Later, the experimental study to determine the control parameters is defined. Finally, the control system is implemented to produce a test geometry. The starting point of the test geometry refers to the pioneering work of Mercelis et al. [34], as these conditions still remain a challenge for the process. The layer-wise control was tested in harsh conditions concerning a large overhang region without any parameter compensation prior to the experiments through empirical or modelling aids. The layer-wise control scheme was able to compensate the overheating observed by the laser heated area enlargement through the tested 5 mm bridged gap from the second layer onward. No control action was applied in the first layer as this layer is used as an observation and learning layer for control in the next layer.

2 Systems and materials

2.1 Open laser powder bed fusion system

The experimental work was conducted on a prototype LPBF system, namely *Penelope*, suitable for research purposes due to the ability to process low powder quantities (up to 500 g) on a small build platform (60x60 mm^2) along with several monitoring capabilities [7]. A single mode fibre laser (IPG Photonics YLR-150/750-QCW-AC, Cambridge, MA, USA) was used in the experiment, characterised by a maximum power of 250 W. The laser could be run in both CW and PW mode with a maximum modulation frequency of 10 kHz. The laser's optical chain initiates with a collimating unit with a focal length of 50 mm, followed by a two-lens focus shifting system (VarioScan 20, Scanlab, Puchheim, Germany), two galvanometric mirrors which deflect the laser beam and a 420 mm f-theta lens, producing a 70 µm theoretical 1/e² beam diameter (d_0) at the focal plane [36]. The scanning parameters and trajectory are set using Scanmaster software (Cambridge Technologies, Bedford, MA). The software made it possible to control process parameters such as scan speed (v), laser peak power (P_{peak}), duty cycle (δ), and pulse repetition rate (PRR) freely at a scan vector level. Controlling the movement of the mechanical system and the chamber pressure is employed in a LabVIEW environment (National Instruments, Austin, TX). The fully automated powder bed is placed in a closed chamber where a controlled inert atmosphere with argon is created. The main specifications for the open LPBF platform and its optical chain can be found in Table 1.

Table 1. Main characteristics of the LPBF platform

Parameter	Value
Laser emission wavelength, λ	1070 nm
Max. laser power, P_{peak}	250 W
Beam quality factor, M^2	1.1
Nominal beam diameter at the focal plane, d_0 (1/e^2)	70 µm

2.2 Coaxial monitoring system and melt pool size indicator extraction

The coaxial monitoring system was designed to acquire thermal emission of the melt pool and maintain the full melt pool within each image. The thermal emission was viewed at NIR range, since the laser optics do not have the transmissivity required at the infrared region. Considering an overestimated melt pool length of 1.5 mm and the laser irradiated point at the centre of the image, the observed region of interest should be larger than 3x3 mm^2. Considering a melt pool width of 0.15 mm, the spatial resolution corresponds to a smaller order of magnitude at approximately 15 μm. The frame rate of the sensor should allow the acquisition of the melt pool at a reasonable rate considering the scan speed and data transfer rate. Considering the scan velocities of the LPBF process and data transfer using a USB 3.0 interface, the frame rate should be higher than 1000 fps [30].

The monitoring setup is mounted co-axially to the scanner head between the galvanometric mirrors and a two-lens focus shifting system (see Fig. 1). The process emission travels through the focusing lens and is reflected by the galvanometric mirrors. The process emission is then reflected by a dichroic mirror transmissive to the laser wavelength, reflective between 400 and 1000 nm towards the sensor (Camera Adapter, Scanlab GmbH, Puchheim, Germany). The process emission is then filtered employing two optical filters limiting the acquisition only to the NIR region between the range of 850 and 1000 nm (FEL0850 and FESH1000, Thorlabs, Newton, NJ, USA). An iris diaphragm is used to control the acquired image intensity. The image is focused on the sensor with a 120 mm focal distance [30]. The same optical chain could be adapted to acquire images of the melt pool with and external illuminator. In this case, a low-coherence light source operating at 640 nm wavelength was employed to reveal the melt pool contour by suppressing the emission of the process (Cavitar, Cavilux HF, Tampere, Finland) substituting the optical filter at the NIR region with a notch-filter at the illuminator's wavelength (FB650-40, Thorlabs, Newton, NJ, USA). An industrial CMOS camera (Ximea xiQ USB Vision, Münster, Germany) was installed, with an 8-bit sensor having a size of 1280 x 1204 pixel and pixel size of 4.8 x 4.8 μm^2. By adapting the region of interest of the sensor, the field of view was adjusted to 4.3 x 4.3 mm^2 with a spatial resolution of 14 μm/pixel, which permits an acquisition rate of 1200 fps with an exposure time of 29 μs.
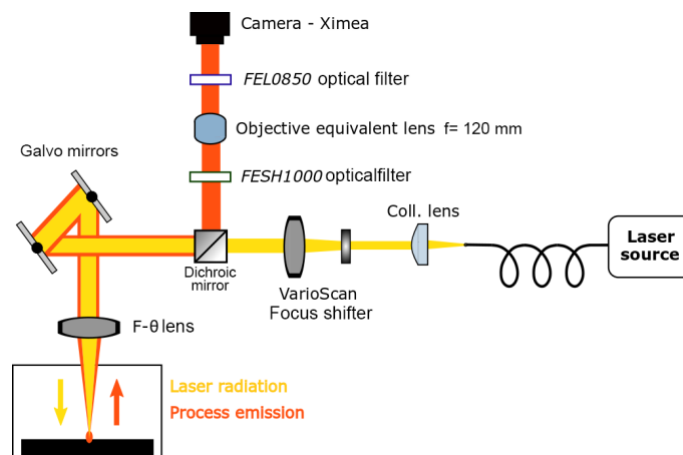

Fig. 1. The optical chain showing the processing laser and the monitored emission paths.

The thermal emission of the melt pool images was acquired using this designed system and transferred to an external PC using the USB 3.0 interface in real-time. Several melt pool indicators can be calculated from each acquired frame. Amongst the different indicators, previous work showed that melt pool area (MPA) is the most informative for showing melt pool size variations due to heat accumulation in thinner sections [19]. A correct calibration of the melt pool size with NIR cameras has several issues related to the plume, spatter formation as well as stray lights in the optical chain [37]. Moreover, as the melt pool and the surrounding areas heat up, the emissivity also varies. Simple thresholding methods can lead to an incorrect estimation of the melt pool dimensions. Especially the melt pool width can be overestimated as compared to *post-mortem* measurements commonly carried out on the metallographic samples. A complete and precise calibration of the monitoring chain could potentially allow the ease of integration to a variety of LPBF systems independent from the optical chains and sensors employed. However, in this work, the attention was towards a simple method to estimate the size of the melt pool and the surrounding heated zone, especially by means of an area indicator rather than a single dimension such as width or length. Hence, with this given imprecision in the melt pool size estimation, the indicator is referred to as laser heated area (LHA). The LHA is a proxy to the MPA possibly overestimating the real melt pool size due to the calibration issues not resolved within this work.

For estimating the LHA value, the image is first binarized performing a static thresholding algorithm. The image binarization and melt pool size estimation were carried out employing the methods developed in the a previous work [38]. The threshold value was chosen by comparing NIR images and images of the melt pool acquired using an external illuminator of the same experimental LPBF conditions [38]. A thin wall (1 mm in thickness) was observed by illuminating the powder bed. The camera images were triggered together with the illuminating laser. Although images were not acquired simultaneously the average size comparisons were considered valid. As shown in Fig. 2.a, the melt pool in the illuminated images could be revealed by the dark blob as the solidified metal appears as the bright reflective surface, while the powder bed remains in between in terms of reflected light intensity. The Density-Based Spatial Clustering of Applications with Noise (DBSCAN) algorithm was employed to apply density-based clustering around the dark zone defined as the melt pool. Once the melt pool is determined by the clustering algorithm the measured area could be matched to the images observed in NIR (Fig. 2.b). In particular, the binarization threshold was determined to minimize the error between the average measurements made with the NIR images compared to those acquired with the external illuminator. In the NIR images, the ejected particles and spatters were distinguished and removed to reveal the melt pool only (Fig. 2.c).
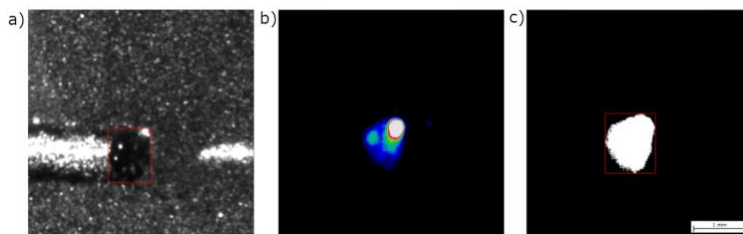
Fig. 2. Determination of the threshold value by comparing the melt pools observed with an external illuminator and the NIR images. a) Image of the melt pool observed with an external illuminator indicated with the red rectangle. b) False-colour image of the melt pool observed in the NIR. c) Binarized image of the melt pool starting from the NIR image corresponding to the same melt pool area.

After these stages the LHA of frame number *k* could be calculated using the following equation:

$$LHA_k[mm^2] = r^2 \cdot \sum_{i=1}^{m} \sum_{j=1}^{n} p^T{}_{k_{i,j}} \qquad (1)$$

where r is the spatial resolution, $p_{k_{i,j}}$ is the gray level of the pixel in row i and column j of the frame k, and $p^T{}_{k_{i,j}}$ is the binary value of $p_{k_{i,j}}$ according to the threshold value.

The method, due to the mentioned imprecisions, proposes different threshold values for melt pool area, width and length since the sizes are determined by geometrical comparison rather than a temperature calibration. The threshold level, found by comparing the same area observed in the externally illuminated and the NIR images, was set to a grey value of 9. For the purpose of estimating the LHA values to be used in the control scheme, the approach was found to be adequate. Fig. 3 depicts the various passages starting from the raw image through to thresholding, spatter elimination, and finally melt pool area extraction. Melt pool size indicators were matched to the scanned position via the use of normalized cross-correlation between images. For this purpose, the powder bed surface was scanned with an external illuminator prior to the LPBF process to acquire the positions for each frame, as explained in [39]. The scan pattern adopted in the experiments in this work was meander. As the scan pattern was not rotated and remained the same throughout all the layers, the same acquired position data was used for all scanned layers of the given geometry. For the short scan trajectories scanned faster than the time required to acquire the consecutive frame (1/1200 fps x 400 mm/s=333 µm) only a single frame could be captured.
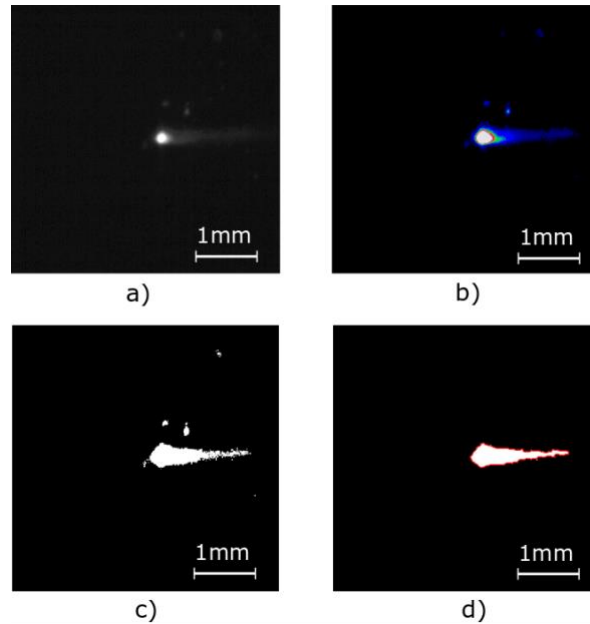
Fig. 3. Image analysis sequence: a) raw image frame acquired during experimentation (the reader is referred to Table 2 for the used fixed process parameters, whereas the employed duty cycle was 1.0 and the scan vector length was 5.0 mm), b) shown in false colours of intensity, c) binarized image, d) image after spatter removal and melt pool identification. Each image shows an observation field of 4.3 x 4.3 mm².

2.3 Material

Stainless steel AISI 316L powder, gas-atomized with nitrogen, was used to conduct the research work (Cogne Acciai, Brescia, Italy). The powder packing density was 4.07 g/cm³, while the powder size distribution is D10: 22.9 µm, D50: 31.9 µm; D90: 44.3 µm.

2.4 Characterization of equipment

For reconstructing the surfaces of the LPBF fabricated parts for geometrical accuracy inspection, a focus variation microscope was used (Alicona Infinite Focus), able to perform a three-dimensional reconstruction of a surface with a maximum vertical resolution of 10 nm. Images were acquired using 5X magnification with estimated vertical and lateral resolutions of 1.1 μm and 7.83 μm, respectively. The images of the surface reconstruction were performed with automatic image stitching which is a build-in automatic feature of the used optical microscope.

3   Layer-wise control strategy

3.1 Definition of system dynamics and control strategy

The use of a real-time control in LPBF is a complex task considering the temporal and dimensional scale of the physical phenomenon involved. Several stages are implemented from signal acquisition through to application of the control command. The image is captured by the monitoring setup, then transferred to the PC, which then carries out the data processing algorithm to calculate the LHA and the control output to be compensated for, which is later sent. The total time required for all these operations was calculated as approximately 1.4 ms employing the USB 3.0 protocol for data transfer. This duration exceeds the period between each frame, i.e. 0.83 ms at the acquisition rate of 1200 fps (see Fig. 4.a). Moreover with a relatively moderate scan speed (v) of 0.4 m/s each observed melt pool is spaced approximately 333 μm (see Fig. 4.b) apart, considerably large compared to melt pool length and width achieved during the process. Consequently, implementing a real-time control system is not feasible here with the general purpose and economic hardware adopted to transfer and process data. Such considerations are coherent with the calculations carried out by Adnan et al [40]. The use of sensors integrated with Field Programmable Gate Array (FPGA) are yet another possibility, which can provide a further reduction of the total time between acquistion and reaction, while remaining in the same *ms* time scale [41]. The limitations of real-time control can therefore be overcome employing a layer-wise control scheme, which is less demanding in terms of data acquistion and reaction time requirements.
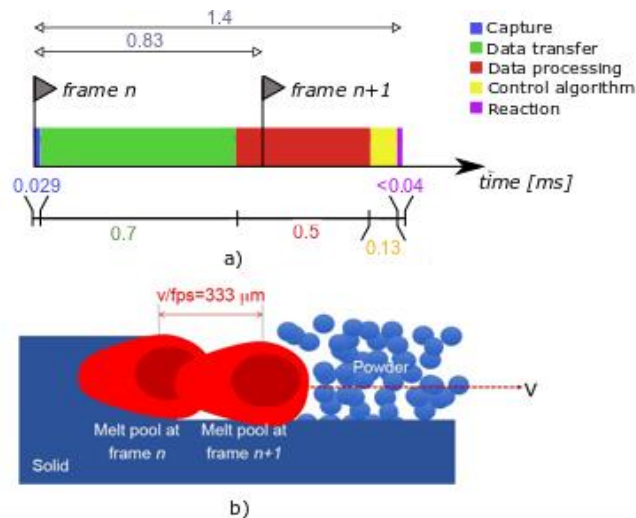

Fig. 4. a) Temporal and b) spatial limitations concerning a closed loop control scheme in the implemented configuration based on a CMOS camera.
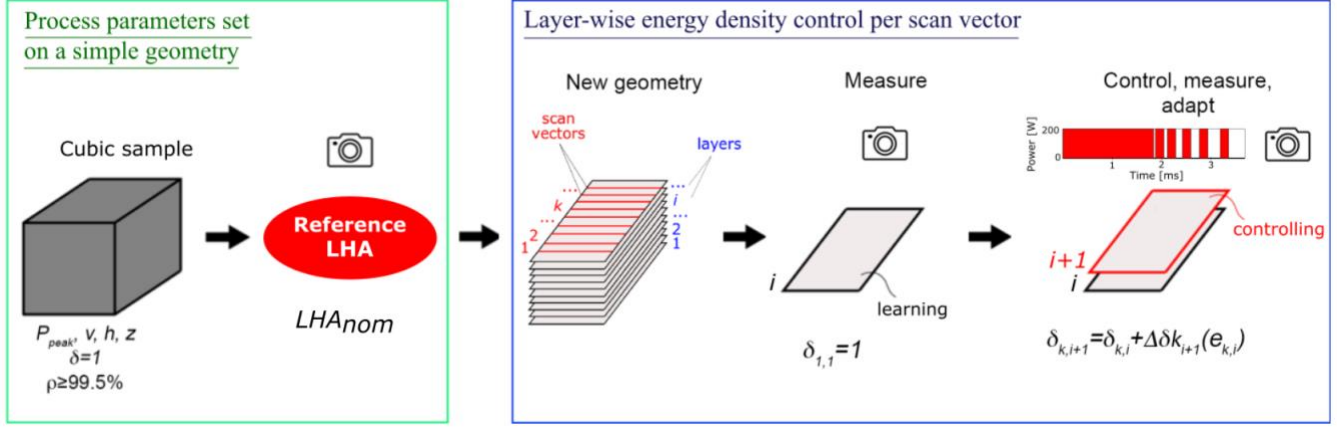
9

Fig. 5. Schematic explanation of the layer-wise control strategy.

The concept of the layer-wise control strategy is to monitor and learn from previous layers in order to correct or limit the propagation of the process defect in the successive layers as schematically shown in Fig. 5. The concept was explained in a previous work [42] for layers built on solid material and in the absence of overhang regions. The strategy consists of managing the energy density input in order to avoide heat accumulation in critical zones of the part's geometry. The laser energy density E is defined as the energy delivered on unit volume material:

$$E = \frac{P_{peak} \cdot \delta}{h \cdot z \cdot v} \qquad (2)$$

where h is the hatch distance, z is the layer thickness, v is the scanning speed, P_{peak} is the peak laser power, and δ is the duty cycle, which is the proportion of the laser emission time (t_{on}) to the total period between consecutive pulses calculated as:

$$\delta = t_{on} PRR \qquad (3)$$

where PRR is the pulse repetition rate defined as the number of pulses emitted per second.

The energy density is controlled by the laser modulation shifting the emission profile from CW towards PW. The modulation profile is controlled by the duty cycle, which appears to be the fastest way to change the energy density compared to the other parameters involved, whereas the PRR remains constant. Layer thickness cannot be changed per scan vector, hatch distance requires reprogramming of all the scan vectors, scan speed adjustments require consideration of the mechanical behaviour of the galvanometric mirrors. On the other hand, the laser peak power could also be controlled, while typically an anological control is employed for this purpose. However, an anological control is intrinsically slower compared to the digital input required for the modulation signal used to control the duty cycle.

The layer-wise control strategy works in that it calculates and evaluates the average melt pool area of the scan vector k in the layer i (LHA,$_i$), and corrects the delivered energy density in the same scan vector k in the subsequent layer $i+1$, by adjusting the duty cycle of the laser power ($\delta_{k,i+1}$). The error of melt pool area for a given layer and scan vector is defined as

$$e_{k,i} = LHA_{nom} - LHA_{k,i} \qquad (4)$$

where LHA$_{nom}$ is the nominal melt pool area for a stable melting condition. In the case when the melting process of a scan vector in the previous layer is optimal ($e_{k,i}$=0), the duty cycle will not be varied ($\delta_{k,i+1}$= $\delta_{k,i}$). For conditions deviating from the nominal melt pool area at layer i, the duty cycle is adjusted at layer $i+1$. The adjusted duty cycle $\delta_{k,i+1}$ is found as a sum of the previous duty cycle $\delta_{k,i}$ and a correction factor $\Delta\delta_{k,i+1}$. The correction factor $\Delta\delta_{k,i+1}$ is computed as a function of the error of the melt pool area $e_{k,i}$.

$$\delta_{k,i+1} = \delta_{k,i} + \Delta\delta_{k,i+1}(e_{k,i}) \qquad (5)$$
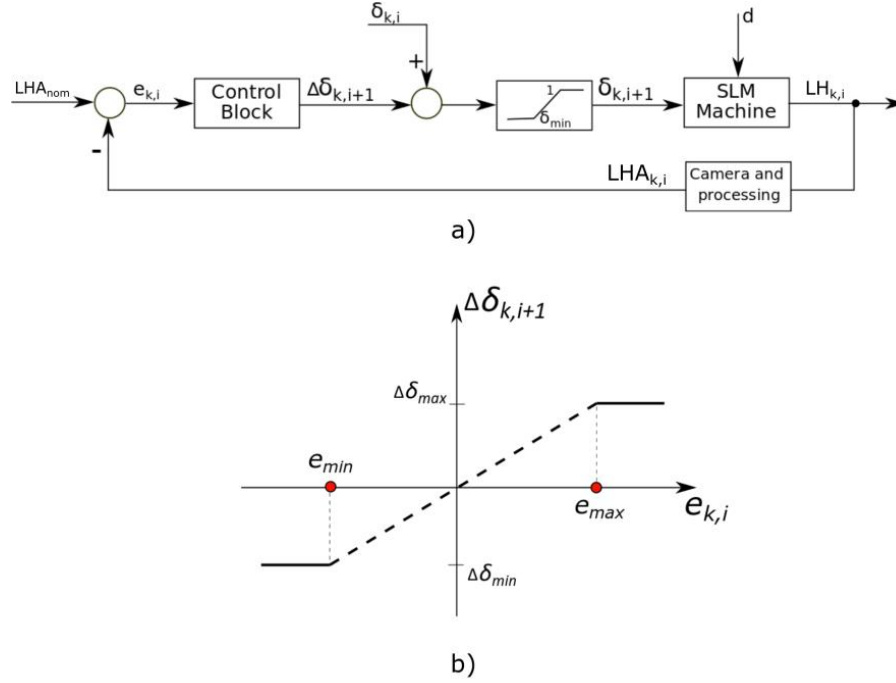
Fig. 6. a) Control scheme, and b) simplified control graph of the layer-wise control strategy.

The control scheme and the graph of the layer-wise control strategy are shown in Fig. 6. For developing the layer-wise control strategy, several parameters should be determined. First, the value of the nominal melt pool area (LHA $_{nom}$), which indicates a stable melting condition, should be determined. Secondly, the dependence between the duty cycle and the length of the scan vectors in critical regions for maintaining steady-state LHA should be identified. Hence, minimum and maximum melt pool size error (e_{min} and e_{max}), and minimum and maximum duty cycle correction factors ($\Delta\delta_{min}$ and $\Delta\delta_{max}$) should be defined. All these unknown parameters were estimated experimentally.

3.2 Choice of the experimental constants

3.2.1 Experimental design for determining the control constants

An experimental campaign, producing square and triangular samples as shown in Fig. 7, was conducted to determine the unknown parameters in the control model. The nominal laser heated area corresponding to a stable

process condition was investigated by scanning a cubic sample with nominal parameters in CW mode, as this was proven to produce >99% apparent part density using the process parameters shown in Table 2. The specimens were printed directly on the baseplate. The baseplate was not heated during the experimental builds. The nominal laser heated area, which was determined by observing the monitoring images of the square shaped sample as the average melt pool area of 30 layers, was found to be 0.46 with a standard deviation of 0.07 mm^2. In stable conditions, employing the NIR images the laser heated area width and length were estimated at approximately 0.43 ± 0.08 mm and 1.56 ± 0.27 mm, respectively (values provided as mean $\pm$ standard deviation calculated). The values were calculated from data obtained over 30 layers containing approximately 1000 frames per layer and excluding the start and end of each scan vector. These dimensions are similar to melt pool sizes observed via thermal imaging declared by Hooper [43] during the LPBF of Ti6Al4V and Lane et al. [44] during the LPBF of Inconel 625. However, in both of the works the authors underlined that the images did not show the exact melt pool dimensions. In particular, Hooper [43] attempted to better highlight the plume and particle ejection in the experimented conditions, while Lane et al [44] stated that the melt pool measurements through these images could not be taken due to the plumes and reflections. On the other hand, the track width was measured with metallographic cross sections and was found at 192 μm with a standard deviation of 15 μm calculated over 10 measurements. Accordingly, the results confirm that the monitoring system is not capable of measuring the real melt pool width, but the measurements are overall adequate indicators to the heating up or underheating conditions generated during the process.
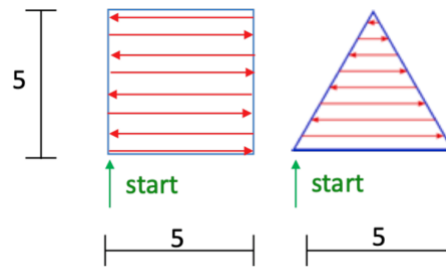

Fig. 7. Scheme of square and triangle shaped samples showing the dimensions in millimetres and the scan direction. Hatch distance of 70 μm was used in the experiment.

Table 2. Process parameters employed in the experiment to determine the control parameters

Fixed parameters	
Layer thickness, z [μm]	50
Hatch distance, h [μm]	70
Scan speed, v [mm/s]	400
Peak power, P_{peak} [W]	200
Pulse repetition rate, PRR [kHz]	3
Scan direction [°]	0
Scan strategy	Meander
Varied parameters	
Duty cycle, δ	0.3 – 1.0
Scan vector length, l_{sv} [mm]	0.05 – 5.0

To determine the control constants, the influence of duty cycle on the laser heated area when heat accumulation occurs due to geometrical variations had to be determined. Such conditions are present when the adjacent scan vectors get shorter towards a pointy edge (see Fig. 7). Therefore, the second part of the experiment involved investigating the effect of variable scan vector length l_{sv} on the laser heated area variation, as a function of the laser energy input. An equilateral triangle with 5 mm side length was chosen as a test geometry which consists of continuously changing scan vector length. The energy input was altered by varying the duty cycle from 0.3 to 1. The melt pool area was measured for each scan vector for 30 layers. The fixed and varied scanning parameters employed in the experiment are summarized in Table 2. An image of the resulting specimens is shown on Fig. 8.
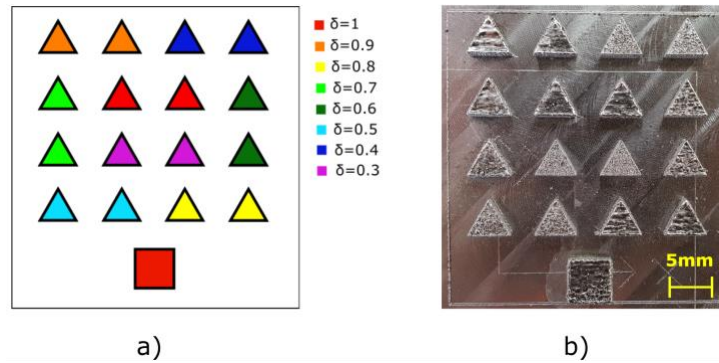
Fig. 8: a) Scheme of the samples' position of the employed duty cycles; b) image of the resulting specimens built with 30 layers.

3.2.2   Parameter choices for the control scheme

Fig. 9 shows spatial colour maps of the LHA of the corresponding scan vector as a function of the duty cycle in a total of 30 layers. The effect of the duty cycles and scan vector lengths on the melt pool area are clearly visualized, concluding that high energy density results in overheating in the pointy edges, whereas low energy density results in under-melting in the longer scan vectors. It can be observed that with high duty cycles the laser heated area can reach areas as large as 1 mm^2 towards the edge of the triangle, where the scan vectors are the shortest. At the edge of the triangle specimens, it is always consistently hotter as visualized on Fig. 9 by the LHA values larger than the nominal. Furthermore, in the initial layers is observed an increase of the MPA. This can be attributed to the fact that in the initial part of the build process the effective layer thickness is smaller. As the process proceeds, the layer shrinkage causes the effective layer thickness to increase to a stable and larger value. With 50 µm layer thickness and approximately 50% powder density converges towards an effective thickness of 100 µm by 7th layer. The smaller effective layer thickness may be a plausible cause for the resultant higher LHA at the start of the build [45].

Fig. 10 shows the stable (Fig. 10.a), under-melting (Fig. 10.b) and over-melting conditions (Fig. 10.c) observed in the experiments. In particular, the over-melting conditions are representative of the heat accumulation observed in real part geometries with hotspot formation. As seen in Fig. 10.c the laser heated area keeps enlarging as the scanned vectors progress towards the edge of the triangle. The heat builds up and the previously scanned vectors remain molten, generating a large apparent melt pool. This heat build-up is one of the main factors contributing to the geometrical deviations such as swelling around the heat accumulated regions.
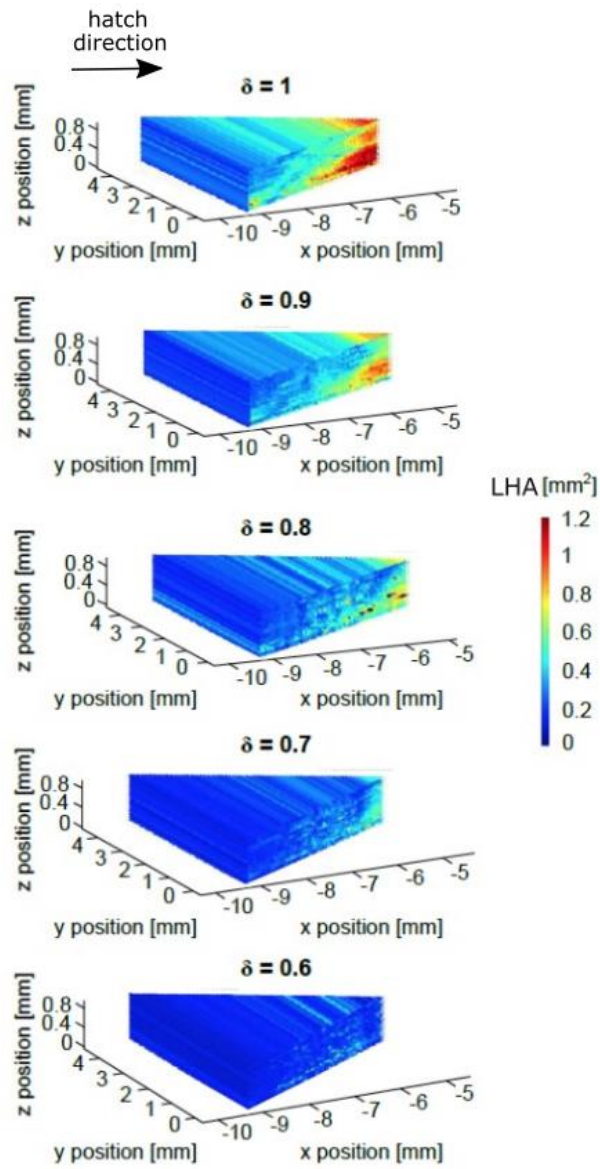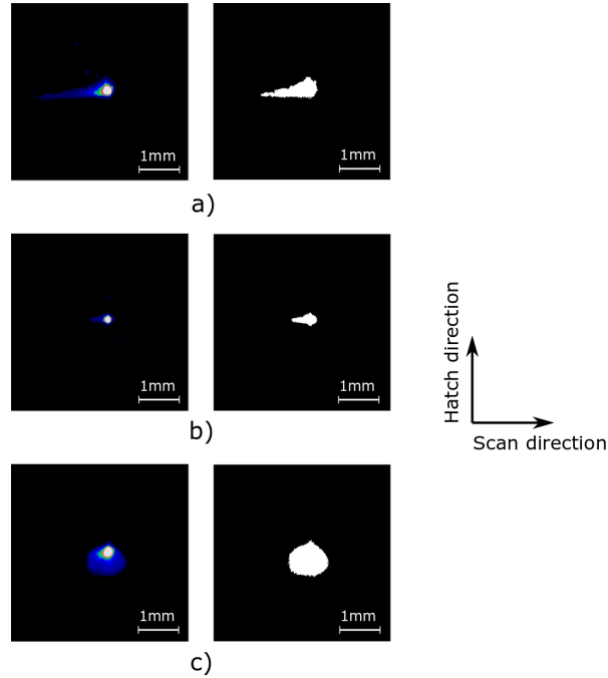
13

Fig. 9. Spatial colour maps of LHA per duty cycle in triangular specimens.

Fig. 10. Melt pool images acquired during scanning the triangle samples shown in false colours of intensity and binarized, depicting: a) stable (long vector scanned with δ=1); b) under-melting (long vector scanned with δ=0.6); c) over-melting (short consecutive vectors scanned with δ=1) conditions. Each image shows an observation field of 4.3 x 4.3 mm².

A regression model was fitted to the average LHA values per scan vector, obtained until the 30th layer, with R_{adj}^2=98.61%. The final equation expressing LHA [mm²] as a function of scan vector length l_{sv} [mm] and laser duty cycle δ was:

$$\ln(LHA) = -3.0153 + 3.843 \cdot \delta - 0.2241 \cdot l_{sv} - 0.860 \cdot \delta^2 + 0.00912 \cdot l_{sv}^2 \qquad (6)$$

The proposed model can be used for offline estimation of the duty cycle as a function of the scan vector length, when considered the same material, equipment, processing conditions and image threshold value, which is not within the scope of this work. On the other hand, the model is not capable of estimating the heat accumulation effects due to overhang structures. Indeed, with the same scan vector length it is possible to scan in an overhang region on the powder or on a solid part. Employing the fitted data, the process stability zone was attained. An acceptable value of LHA variability was tentatively sought at a variation of ±2% corresponding to ±0.01 mm². Fig. 11 shows the regression equation solved to depict the stable region on top of the contour plot of the regression equation. The stable process window shows the optimal duty cycle of the laser power as a function of the scan vector length. From the contour plot, it is determined that there is no apparent advantage to modulating with a duty cycle much less than 0.7, since with duty small values of duty cycle insufficient melting is observed without a significant change in the laser heated area.
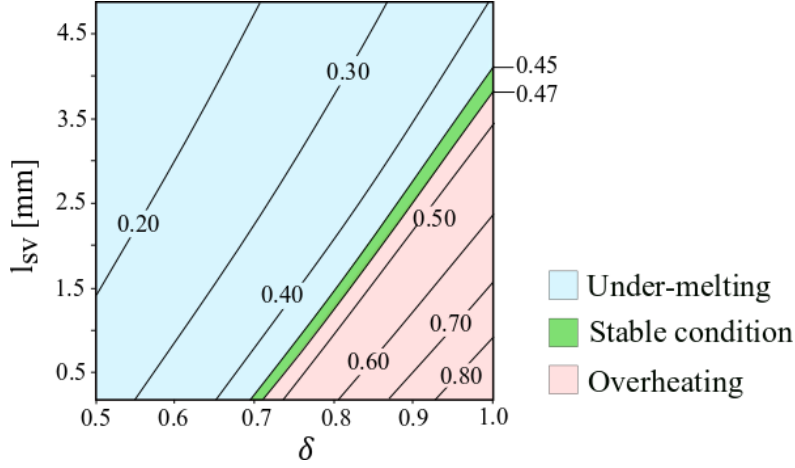
Fig. 11. Contour plot of the regression model showing iso-curves of LHA [mm²]. The under-melting, stable, and overheating zones are shaded in different colours.

Therefore, to provide a larger margin of intervention for the control scheme, the minimum duty cycle employed for laser power modulation was set to $\delta_{min}=0.6$. The maximum duty cycle is when the laser runs at CW, hence $\delta_{max}=1$. Thus, the maximum and minimum compensation factor for the duty cycle can be found as follows:

$$\Delta\delta_{max} = \delta_{max} - \delta_{min} = 1 - 0.6 = 0.4 \qquad (7)$$

$$\Delta\delta_{min} = \delta_{min} - \delta_{max} = 0.6 - 1 = -0.4 \qquad (8)$$

The compensation factor is provided as an output of the control block (Fig. 6).

According to Equation (5) for specific values of the compensation factor $\Delta\delta_{k,i+1}(e_{k,i})$, the new duty cycle $\delta_{k,i+1}$ can reach values higher than 1 and lower than 0.6. For that reason, the control output in the model was saturated between the values of 0.6 and 1.

The process window of the contour plot in Fig. 11 demonstrates that when the scan vector length decreases below 4 mm, modulation of the laser power is required to maintain optimal energy input and avoid overheating. When lengths longer than 4 mm are scanned, the scan vector length does not affect the melt pool, therefore a CW mode with the optimized fixed parameters shown on Table 2 is employed in this range.

The input of the control block is defined as the melt pool area error ($e_{k,i}$) of the scan vector k in layer i (see Equation (4). The error is at its maximum (e_{max}) when the minimum melt pool area (LHA$_{min}$) is reached. LHA$_{min}$ is found as the average of the smallest melt pool areas noted in the experiment, corresponding to the insufficient melting region of the triangles (largest scan vector lengths scanned with the lowest duty cycle $\delta=0.6$), and it is equal to 0.16 mm².

The maximum LHA error (e_{max}) is computed as follows:

$$e_{max} = LHA_{nom} - LHA_{min} = 0.46 - 0.16 = 0.3 \ mm^2 \qquad (9)$$

16

The minimum error value (e_{min}) indicates that the maximum laser heated area (LHA$_{max}$) is reached. LHA$_{max}$ is found to be the average of the largest melt pool areas noted in the experiment, corresponding to the heat build-up regions of the triangles (shortest scan vector lengths scanned with δ=1), and it is equal to 0.94 mm^2.

The minimum LHA error is computed as follows:

$$e_{min} = LHA_{nom} - LHA_{max} = 0.46 - 0.94 = -0.48 \ mm^2 \qquad (10)$$

For completing the control model, it is necessary to define the relationship between the duty cycle and the melt pool area. Tentatively, the control curve of the correction factor of the duty cycle and the melt pool area error are approximated as a linear function.

The control scheme with all the established parameters is shown in Fig. 12. The disturbances acting on the melt pool (MP) related to other factors such as the material or gas flow are denoted with d in the control scheme. The control block of the control scheme works in such a way that it computes the duty cycle correction depending on the LHA error. In Fig. 12, the control graph of the change of duty cycle as a function of the melt pool area error is shown. The output it gives is the maximum duty cycle correction $\Delta\delta$=0.4 in cases where there is extreme insufficient melting and the laser needs to operate in CW mode, and its output provides the minimum duty cycle correction $\Delta\delta$=-0.4 when there is excessive overheating in the scan vector, which results in the need to decrease the duty cycle to the minimum. In between these two extreme values, the correction factor for the duty cycle is calculated linearly as a function of the error. The error has zero value when the nominal melt pool area has been reached, and the duty cycle of scan vector k of the previous layer i is retained for the scan vector k of the following layer $i+1$ ($\delta_{k,i+1}=\delta_{k,i}$).
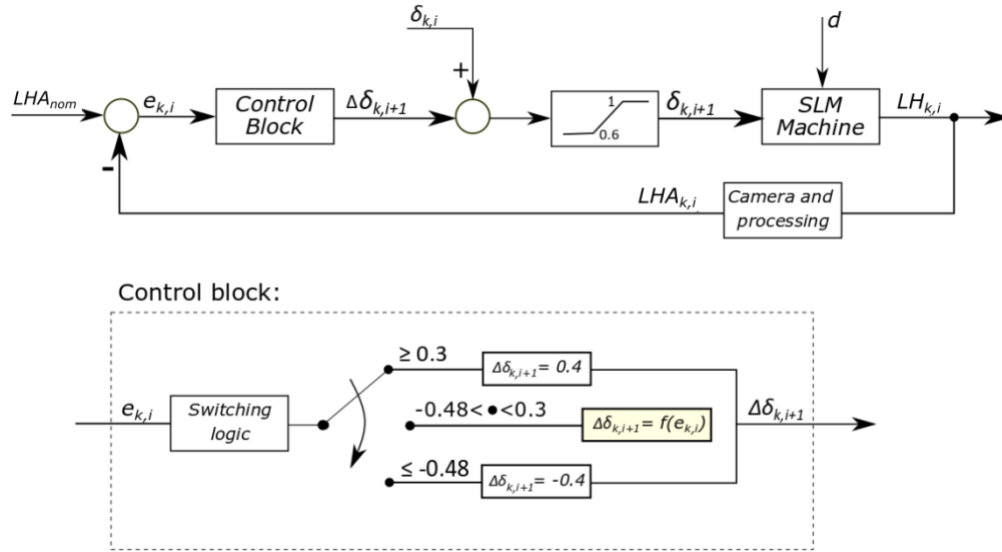

Fig. 12. The final configuration of the layer-wise control scheme with the control block used.

4 Layer-wise control of melt pool area on overhang structures

The layer-wise strategy was employed previously to detect and compensate for the heat accumulation due to the small scan vectors around the pointy edges [42]. In the case of an overhang structure, the scan vector can be sufficiently long to avoid heat accumulation, but the absence of solid metal to transfer heat generates a larger melt

17

pool. Hence, the volume of the melt pool significantly expands. The melt pool area increases at the scanning surface as can be monitored by the camera; furthermore, the melt pool can increase in the downward direction where it can sink into the powder beneath it due to gravity and capillary forces. This can lead to the collapse of the overhang surface, or even failure of the whole component. To test the feasibility of the layer-wise control strategy, a simple test geometry reproducing an overhang structure was designed and produced. The overhang structures require supporting due to the reduced thermal conduction within the powder bed. Downskin parameter sets are useful for avoiding heat accumulation. However, they are not meant to compensate for the effects of heat accumulation on overhang regions. Without supports, overheating on the overhangs and bridged gaps is expected to generate a larger melt pool. In the proposed strategy, the monitoring system can assess the melt pool enlargement through laser heated area error and compensate on the overhang region by modulating the laser over the successive layers.

4.1 Experimental design

Table 3 shows the process parameters employed in the experiment, whereas the geometry of the chosen overhang structure and the scanning strategy are shown in Fig. 13. The scan direction was not varied between layers in this work as this simplifies the control approach compared to a situation where the scan vectors are rotated in each successive layer. The build was separated into three zones. Layers in zone number 1 and 3 are supported by solid material during the print, while zone number 2 is a bridged gap of 5 mm sustained on the powder. Throughout the production of the test geometries, the monitoring module acquired the images. For the specimen where the layer-wise control was applied, corrected duty cycle values were fed to the scanner control prior to each layer. Pseudo-tomographic laser heated area maps were produced at the end of the tests. The geometrical deviations on the produced specimens were analysed using focus variation microscopy.

Table 3. Process parameters employed in the validation experiment

Fixed parameters	
Layer thickness, z [µm]	50
Hatch distance, h [µm]	70
Scan speed, v [mm/s]	400
Peak power, P_{peak} [W]	200
Pulse repetition rate, PRR [kHz]	3
Scan direction [°]	0
Scan strategy	Meander
Initial duty cycle, δ	1
Varied parameters	
Control strategy	None; Layer-wise
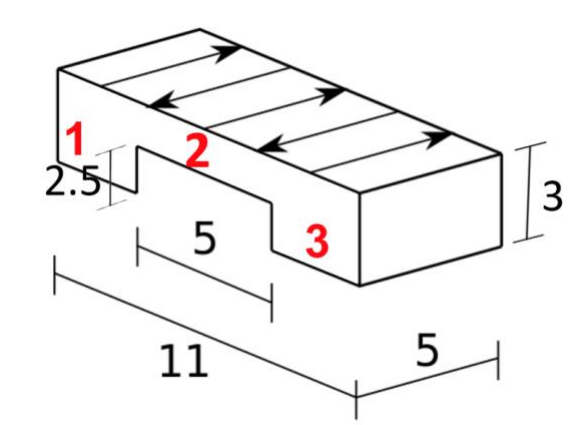
Fig. 13. Geometry of the overhang specimen showing the different zones. Zones number 1 and 3 are supported by solid material during the build, while zone number 2 is the bridged gap. Dimensions indicated in mm.

4.2 LHA maps

The behaviour of the LHA when the bridged gap portion of the samples (zone 2) was produced is shown in Fig. 14. The initial evolution of the LHA for the whole scanned layer (zones 1, 2, and 3 in Fig. 13) is shown in Fig. 14.a. It can be shown that starting from layer 2 the layer-wise control strategy maintains a stable melt pool behaviour. On the other hand, overheating is observed even at layer 10 without the control active. Fig. 14.b shows the stacked LHA maps over height for the bridged gap region (region 2 in Fig. 13). In the absence of a control regime, the heat accumulation progresses over the consecutive layers despite the increased solid mass, which can act as a heat sink.

It can be noted that when the laser scans the overhang region in the bridged gap, the laser heated area can enlarge up to 5 mm^2. This is due to the heat build-up in the region elongating the melt pool to the consecutive vector scans. The largest melt pool area is reached towards the medium section of the overhang, indicating a local equilibrium. Once the scanned track reaches zone 3, the thermal conduction is improved shrinking the melt pool towards the desired size. Fig. 15.a shows NIR images over the overhang region without the layer-wise control. It can be noted that the laser heated region remains elongated due to the non-solidified previous tracks. The limited heat conductivity of the powder bed slows the solidification rate, generating an apparently long melt pool as observed in the pointy edges of the triangular shapes. Despite the different surrounding material mass and physical properties, the heat accumulation in pointy edges and overhang regions appears in a similar, yet somewhat different, fashion. Indeed, the pointy edges compared to the overhang region benefit from better thermal conduction with the solid metal from the previously scanned layers. The overhang region generates a large amount of local heat accumulation, and therefore melt pool mass, due to the worse thermal conduction of the powder. Without the layer-wise control, the melt pool enlargement remains consistent after multiple layers until enough material has been built up. On the other hand, the layer-wise control achieves a stable melt pool behaviour starting from layer number 2, where it is effectively being used as seen in Fig. 15.b. The lack of heat conductivity is compensated for by the reduction of the energy input as targeted by the control scheme.

Fig. 16.a shows the average LHA values along with the standard deviations per layer starting from the first layer scanned in the overhang region. It can be noted that the thermal behaviour of the melt pool in the overhang scanned with fixed parameters starts to stabilize as the number of layers increases. The previously melted layers act as a heat sink and thermal conduction with the existing regions 1 and 2 are better established. Although a stable LHA level is achieved without the control, after 10 layers the average LHA is twice the nominal value and a large variation is observed within the layer. On the other hand, in the specimen produced with layer-wise control, a stabilization of the LHA in the whole layer can be noticed already from the first layer when the control is enabled, i.e. the second layer. It can be observed that the melt pool area starting from the second layer and ongoing, stayed close to the optimal value and was kept stable throughout all the subsequent layers. The variability within the layer is also limited and constant once the layer-wise control starts to be employed.

In Fig. 16.b. the temporal behaviour of the melt pool area during the execution of layer number 3 of the overhang region is presented. It can be seen that, without control, zone 2 has a very large LHA with a large variation between the scanned vectors. It can also be seen that melt pool area deviates from the nominal one throughout the process, indicating an overall thermal accumulation exceeding through the layers. With the layer-wise control no difference between the overhanging region and regions connected to the baseplate is visible. Moreover, the melt pool area remains stable between the layers.
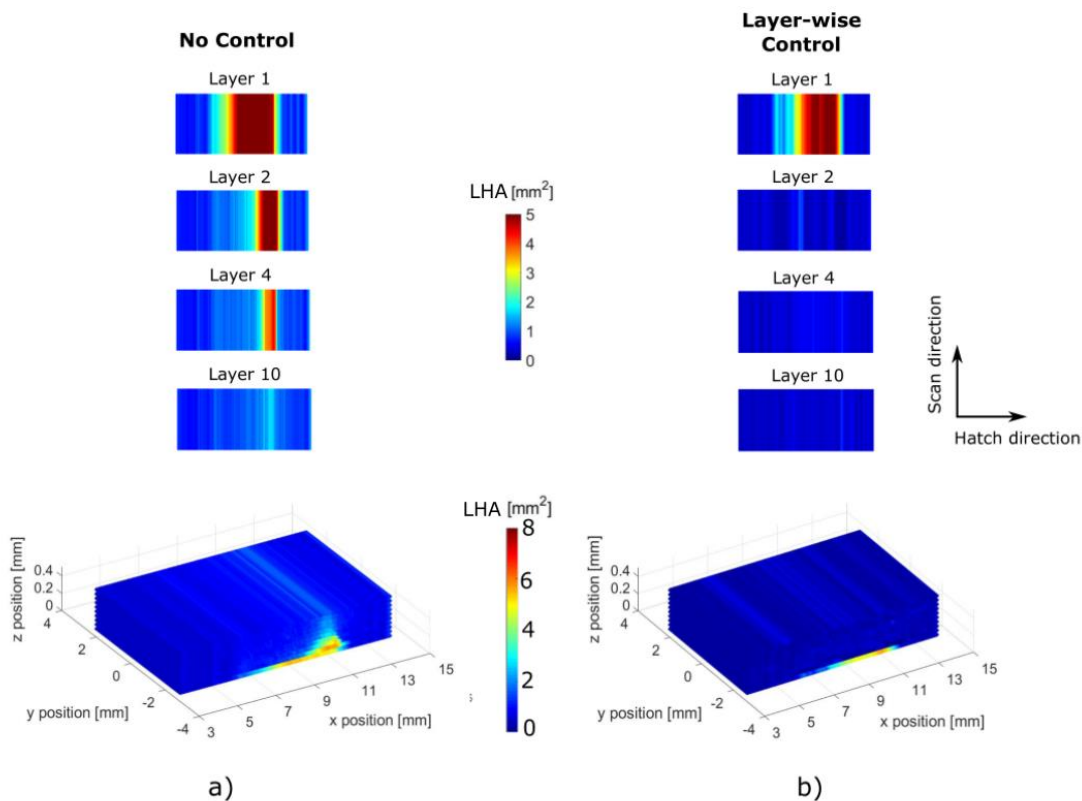
Fig. 14. Spatial colour maps of LHA of the test specimens during the production of the overhang region. a) Specimen produced without control; b) specimen produced with layer-wise control. The figures shown comprise zones 1,2, and 3.
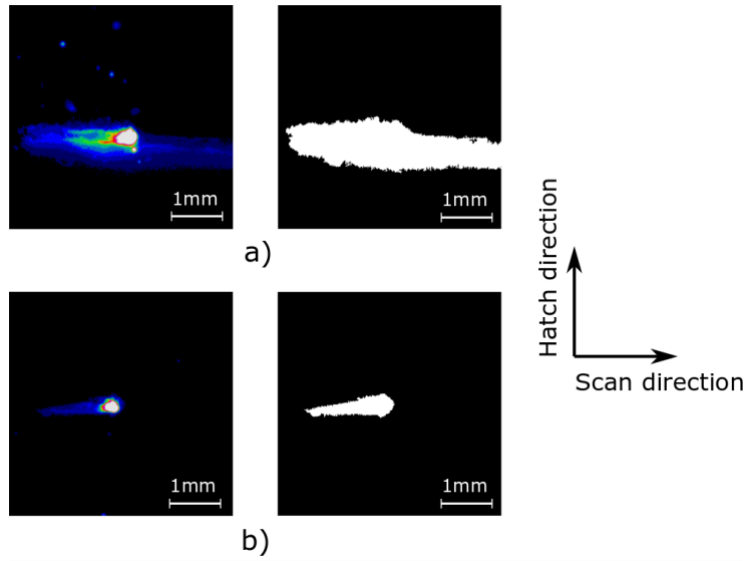
Fig. 15: Melt pool images acquired during scanning the bridged gaps at layer 4, shown in false colours and binarized, depicting: a) over-melting (no control employed); b) stable (layer-wise control employed) conditions.
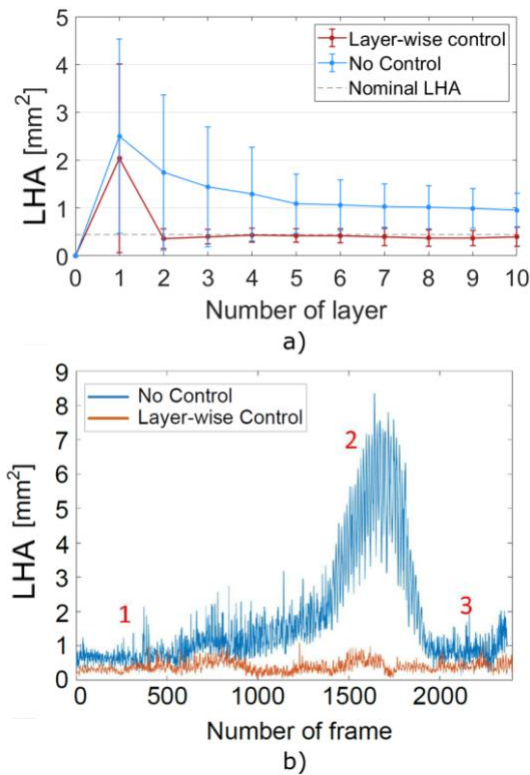

Fig. 16. a) Comparison of LHA values between layers produced without and with layer-wise control (error bars represent standard deviation). b) LHA temporal behaviour during layer number 3 comparing the process without and with layer-wise control (numbers in red indicate the scanned zones on the part).

4.3 Surface morphology and geometrical errors

A three-dimensional reconstruction of the top surface of the samples are shown in Fig. 17. The images show the surface of the whole sample, including zones 1,2, and 3 after 10 layers have been built. It can be seen that without

the layer-wise control the upper surface of the bridged gap (corresponding to zone 2) tends to deteriorate, and its middle part is found to be below the nominal height level (Fig. 17.a). Consequently, the bottom surface also collapses. The first layer of the bridge lowers into the powder below as a result of high energy input, and consequently the level of the support material for the following layers will be found to be lower in the central part of the bridge. Without the layer-wise control the surface flatness is compromised not only in the bridged gap zone 2, but also in zones 1 and 3, which are connected to solid parts. The use of layer-wise control appears to improve geometry and avoid overheating phenomena in overhang regions (Fig. 17.b). The partial surface drop is observable in the transition zone between zones 2 and 3. This local defect happened as a result of the transition between powder and solid which, it is probable, was not fully compensated with the regression correlation model, and the sagging which occurred on the overhang region (zone 2) took up material from the link and then progressed the suction. 3D reconstructions were employed to calculate the height compared to a flat surface as seen in Fig. 17.c. It can be seen that the error values are skewed towards negative values without the control. This indicates that the surface collapse has progressed towards the upper layers, generating a marked surface concavity. The root mean square, maximum, and minimum error values were 170 µm, -714 µm, and 586 µm without control. The mean, maximum, and minimum error values were 58 µm, -484 µm, and 292 µm with the layer-wise control, corresponding to an improvement of the surface flatness and of mean error of approximately 67%.

a)

b)

c)
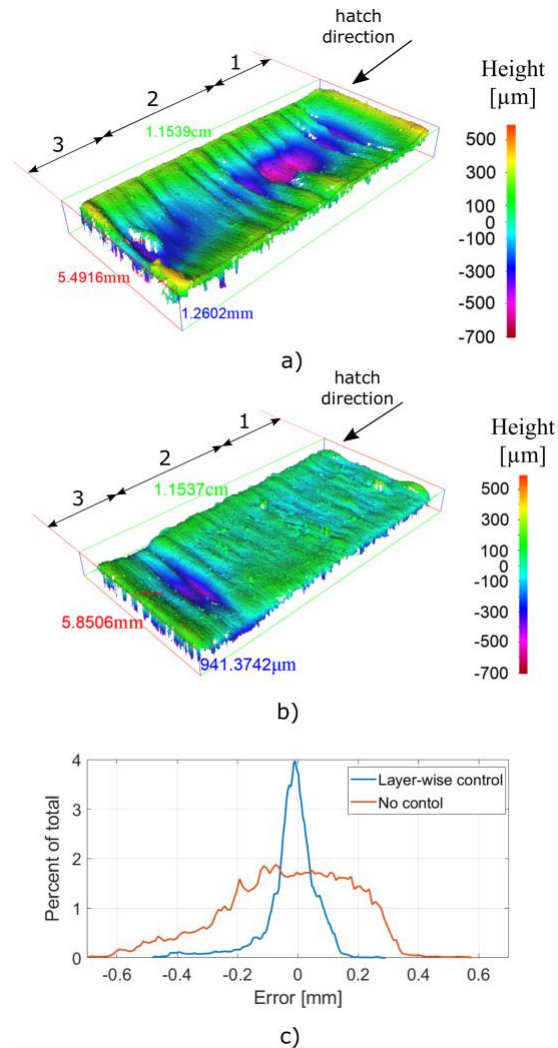
Fig. 17. 3D reconstructions of the whole upper surfaces of the specimens obtained a) without control, and b) with layer-wise control after deposition of 10 layers. c) Surface height error distribution of the specimens.

5 Discussion

The experimental work showed that melt pool enlargement and heating up around the melt zone are indicators of the geometrical deviations that can be expected during layer-by-layer building up of the material. This is coherent with the observations in literature [46]. In the experiments, two distinct cases were used to develop the control model and test it, namely the triangle and the bridged gap. It was observed that heat accumulation can be due to the reduced conductivity as well as reduced wait time between consecutive scan vectors. The resulting enlargement of the melt pool is marked at the bridged gap as the powder bed conducts much less than the solid metal [47] and the released energy is larger compared to the thinner regions. The optical penetration depth of the laser is also expected to be larger when the laser scans the powder bed [48]. As a combination, the local temperatures are expected to rise, excessively enlarging the melt pool [3]. The low conductivity is also expected to play a role in lowering the solidification rate. Hence, the melt pool remains liquid for a longer time. As a result, sagging, warpage and dross accumulation can occur, while in this work the test geometry was found to be compromised on the upper surface as well even after 10 layers of scanning without any control. The experimental work confirms that controlling the energy released in consecutive layers can reduce defect propagation. The use of duty cycle parameter from this perspective is highly appealing as it can be controlled faster than the laser peak power [49]. The use of scan speed or beam size for the same purpose required the manipulation of the mechanical elements such as the galvanometric mirrors and the positioning of a zoom optic. Their manipulation in real-time can be more complex due to the mechanical inertia involved.

Although the efficacy of the layer-wise control strategy has been shown to be effective after the first layer of its use, evidently the prior layer that is used for learning the duty cycle requirements remains an issue. In the scheme presented, the paper shows how the propagation of geometrical error will vanish more rapidly. Due to the initial sagging on the overhang region, in the initial controlled layers there is the possibility that the layer thickness enlarges, and the control works on larger layer thickness. This might impose pores due to lack of fusion, however at this point the model has not been validated for porosity defect but solely for geometrical deviations. Furthermore, the defect generated at the first layer will remain. However, if defect progression can be stopped rapidly, further deterioration can be avoided making it possible to finish a build job without complete failure. Within this work no compensation in terms of downskin parameters or parameter estimation through modelling was employed. Combined with these approaches and starting from lower energy conditions in the overhang regions, the layer-wise control strategy can ensure the quality of the overhang regions, independently of the scanned geometries and reduce the necessity of support structures.

Scan rotation was also not applied within this work. Future implementation should incorporate the correction on a position basis rather than the scanned vector. The position read out is available to most industrial scanner systems. Combined with the position information, the duty cycle can be varied within the scan vector in order to compensate melt pool enlargement on the successive layer. The vectors can also be segmented according to the duty cycle variations. This can reduce the complexity of duty cycle control with position feedback in real-time, by applying the calculation between the layers during the recoating time.

Another issue is related to the calibration methods employed. The work showed that while the NIR images provide useful information for process monitoring and control, they were not calibrated in a correct manner to measure the real melt pool size. This was confirmed with the overestimation of the melt pool width. The calibration stage was further analysed employing the melt pool width measured with the metallographic cross-sections. The binarization threshold was adapted to match the melt pool width measured in the cross-sections and the size measured with NIR images. The results, which are not reported here for the sake of brevity, showed that the LHA indicator was overall much smaller and deviated from the nominal levels less frequently despite the evident defect progression. Despite the high sensitivity to the thresholding selection, the results are promising for defect mitigation. Indeed, the sensitivity of the threshold selection limits the transferability of the method to other LPBF systems with different optical chains and sensors. Nonetheless, an important aspect is that the Laser Heated *Area*, and not its *length* or *width*, is the extracted feature defined as the controlled variable, and therefore it is less sensitive to the threshold value. Then, if the threshold value is found in a selected optimal range, the control system will not be significantly sensitive to the error. If the threshold value is not within a nominal range, the signal can become either non-dynamic or too dynamic. Therefore, the initial step in this work was selecting the proper threshold which will not exhibit bad dynamics of the extracted signal, and such that the variations of the error will not have big impact on the control output.

6 Conclusions

This work demonstrated the use of a layer-wise control strategy to maintain a stable melt pool area and hence avoid surface defects during the production of overhang structures. Coaxial melt pool images were elaborated per layer and per scan vector to correct the laser duty cycle for each scan vector of the successive layer. The required control constants were experimentally determined for AISI 316L stainless steel. The surface integrity of the specimen scanned with controlled laser energy input could be improved significantly. The main outcomes of the work are as follows:

- Real-time control of LPBF via control of laser related process parameters is a challenging task. The calculation and reaction times associated with the control schemes render applicability very limited. Instead a layer-wise control strategy is much slower in principle but can be effective in terms of slowing or stopping defect propagation.
- Laser duty cycle is an effective parameter for controlling the melt pool size. The correct energy density values for avoiding heat accumulation should also consider avoiding undermelting due to an overcompensation action generated by the control scheme. The determination of the extreme values can be carried out using an empirical approach. Such an approach can be a compromise between time consuming simulations and large experimental campaigns to set the correct energy density settings for different geometries.
- The layer-wise control strategy was able to slow down the progression of sagging and surface collapse defects on overhang regions starting from the second layer of the execution of this zone. The same defects require many more layers without the use of any control action. Such defects without any control action can cause the failure of the entire build due to defect propagation to the entire powder bed. Therefore, despite its slower action times, the layer-wise control strategy proves to be an effective method for stopping the progression of certain defects and hence is a feasible approach for closed-loop control.
- The proposed control strategy is based on the use of conventional, off-the-shelf sensors and optics with a relatively low cost, while laser emission modulation is applicable to the vast majority of the fibre laser sources used in the LPBF systems. Hence, the solutions provided are appealing and affordable for

retrofitting on existing LPBF machines. Despite these advantages the calibration of the NIR images remain a sensitive point that requires a more comprehensive methodology for a wider use in the industry.

In this work several aspects were not considered, which were left out for future development. For instance, in industrial practice, the scan vector orientation is rotated commonly by 67° or 90° between successive layers to evenly distribute the tracks along the build direction. As this work indicates feasibility, the use of spatial information to correct rotated scan tracks should be studied further. Indeed, the change of vector angle requires strategies for allocating the duty cycle by position rather than the vector itself. Within this work, the bridged gap region was processed with the same parameter as that used for the bulky regions. Conventionally, downskin parameters are used for this purpose, which can reduce heat accumulation to a certain extent. Hence, the layer-wise control strategy shows further potential when combined with downskin parameters and/or simulations. Such combinations should provide further improvement to the process stability.

Acknowledgements

References

[1]   M. Grasso and B. M. Colosimo, "Process defects and *in situ* monitoring methods in metal powder bed fusion: a review," *Meas. Sci. Technol.*, vol. 28, no. 4, p. 044005, 2017.

[2]   G. Tapia and A. Elwany, "A Review on Process Monitoring and Control in Metal-Based Additive Manufacturing," *J. Manuf. Sci. Eng. Trans. ASME*, vol. 136, no. 6, 2014.

[3]   M. Pavlov, M. Doubenskaia, and I. Smurov, "Pyrometric analysis of thermal processes in SLM technology," *Phys. Procedia*, vol. 5, no. PART 2, pp. 523–531, 2010.

[4]   P. Lott, H. Schleifenbaum, W. Meiners, K. Wissenbach, C. Hinke, and J. Bültmann, "Design of an optical system for the in situ process monitoring of Selective Laser Melting (SLM)," *Phys. Procedia*, vol. 12, no. PART 1, pp. 683–690, 2011.

[5]   N. Eschner, L. Weiser, B. Häfner, and G. Lanza, "Development of an Acoustic Process Monitoring System for Selective Laser Melting (SLM)," *Solid Free. Fabr. Symp.*, no. Reschetnik 2017, pp. 2097–2117, 2018.

[6]   B. A. Fisher, B. Lane, H. Yeung, and J. Beuth, "Toward determining melt pool quality metrics via coaxial monitoring in laser powder bed fusion," *Manuf. Lett.*, vol. 15, pp. 119–121, 2018.

[7]   B. M. Colosimo, E. Grossi, F. Caltanissetta, and M. Grasso, "Penelope: A Novel Prototype for In Situ Defect Removal in LPBF," *Jom*, vol. 72, no. 3, pp. 1332–1339, 2020.

[8]   F. Caltanissetta, M. Grasso, S. Petrò, and B. M. Colosimo, "Characterization of in-situ measurements based on layerwise imaging in laser powder bed fusion," *Addit. Manuf.*, vol. 24, no. August, pp. 183–199,

2018.

[9]   J. A. Kanko, A. P. Sibley, and J. M. Fraser, "In situ morphology-based defect detection of selective laser melting through inline coherent imaging," *J. Mater. Process. Technol.*, vol. 231, pp. 488–500, 2016.

[10]   R. J. Smith, M. Hirsch, R. Patel, W. Li, A. T. Clare, and S. D. Sharples, "Spatially resolved acoustic spectroscopy for selective laser melting," *J. Mater. Process. Technol.*, vol. 236, pp. 93–102, 2016.

[11]   A. A. Martin *et al.*, "Dynamics of pore formation during laser powder bed fusion additive manufacturing," *Nat. Commun.*, vol. 10, no. 1, pp. 1–10, 2019.

[12]   N. H. Paulson, B. Gould, S. J. Wolff, M. Stan, and A. Greco, "Correlations between thermal history and keyhole porosity in laser powder bed fusion," *Addit. Manuf.*, no. March 2020, p. 101213.

[13]   M. Grasso, V. Laguzza, Q. Semeraro, and B. M. Colosimo, "In-Process Monitoring of Selective Laser Melting: Spatial Detection of Defects Via Image Data Analysis," *J. Manuf. Sci. Eng.*, vol. 139, no. 5, p. 051001, 2016.

[14]   V. Finazzi *et al.*, "Design Rules for Producing Cardiovascular Stents by Selective Laser Melting: Geometrical Constraints and Opportunities," *Procedia Struct. Integr.*, vol. 15, pp. 16–23, 2019.

[15]   S. A. Khairallah *et al.*, "Controlling interdependent meso-nanosecond dynamics and defect generation in metal 3D printing," *Science (80-.).*, vol. 368, no. 6491, pp. 660–665, 2020.

[16]   L. Caprio, A. G. Demir, and B. Previtali, "Influence of pulsed and continuous wave emission on melting efficiency in selective laser melting," *J. Mater. Process. Tech.*, vol. 266, no. November 2018, pp. 429–441, 2019.

[17]   A. G. Demir and B. Previtali, "Additive manufacturing of cardiovascular CoCr stents by selective laser melting," *Mater. Des.*, vol. 119, 2017.

[18]   A. G. Demir, P. Colombo, and B. Previtali, "From pulsed to continuous wave emission in SLM with contemporary fiber laser sources: effect of temporal and spatial pulse overlap in part quality," *Int. J. Adv. Manuf. Technol.*, vol. 91, no. 5–8, pp. 2701–2714, 2017.

[19]   A. G. Demir, L. Mazzoleni, L. Caprio, M. Pacher, and B. Previtali, "Complementary use of pulsed and continuous wave emission modes to stabilize melt pool geometry in laser powder bed fusion," *Opt. Laser Technol.*, vol. 113, no. October 2018, pp. 15–26, 2019.

[20]   J. T. Hofman, B. Pathiraj, J. Van Dijk, D. F. De Lange, and J. Meijer, "A camera based feedback control strategy for the laser cladding process," *J. Mater. Process. Tech.*, vol. 212, no. 11, pp. 2455–2462, 2012.

[21]   L. Song and J. Mazumder, "Feedback control of melt pool temperature during laser cladding process," *IEEE Trans. Control Syst. Technol.*, vol. 19, no. 6, pp. 1349–1356, 2011.

[22]   J. R. Duflou, E. F. Sichani, J. De Keuster, and K. U. Leuven, "Developemenf of a real time monitoring and adaptive control for laser flame cutting," *J. Laser Appl.,* 527, 2009

[23]   S. Postma, R. G. K. M. Aarts, J. Meijer, B. Jonker, and W. M. Zweers, "Penetration control in laser welding of sheet metal using optical sensors," vol. 210, no. November 2001, pp. 1083–1092, 2018.

[24]   J.-P. Kempen, Karolien, Vrancken, Bey, Thijs, Lore, Buls, Sam, Van Humbeeck, Jan, and Kruth, "Lowering thermal gradients in selective laser melting by pre-heating the baseplate," *Solid Free. Fabr. Symp. Proc.*, 2013.

[25]   A. G. Demir and B. Previtali, "Investigation of remelting and preheating in SLM of 18Ni300 maraging steel as corrective and preventive measures for porosity reduction," *Int. J. Adv. Manuf. Technol.*, vol. 93, no. 5, pp. 2697–2709, Nov. 2017.

[26]   Z. Li, R. Xu, Z. Zhang, and I. Kucukkoc, "The influence of scan length on fabricating thin-walled components in selective laser melting," *Int. J. Mach. Tools Manuf.*, vol. 126, no. November 2017, pp. 1–12, 2018.

[27]   K. Zeng, D. Pal, H. J. Gong, N. Patil, and B. Stucker, "Comparison of 3DSIM thermal modelling of selective laser melting using new dynamic meshing method to ANSYS," *Mater. Sci. Technol. (United Kingdom)*, vol. 31, no. 8, pp. 945–956, 2015.

[28]   M. Bugatti and Q. Semeraro, "Limitations of the inherent strain method in simulating powder bed fusion processes," *Addit. Manuf.*, vol. 23, no. June 2017, pp. 329–346, 2018.

[29]   C. L. Druzgalski, A. Ashby, G. Guss, W. E. King, T. T. Roehling, and M. J. Matthews, "Process optimization of complex geometries using feed forward control for laser powder bed fusion additive manufacturing," *Addit. Manuf.*, p. 101169, 2020.

[30]   L. Mazzoleni, A. G. Demir, L. Caprio, M. Pacher, and B. Previtali, "Real-Time Observation of Melt Pool in Selective Laser Melting: Spatial, Temporal and Wavelength Resolution Criteria," *IEEE Trans. Instrum. Meas.*, pp. 1–1, 2019.

[31]   V. Renken, A. von Freyberg, K. Schünemann, F. Pastors, and A. Fischer, "In-process closed-loop control for stabilising the melt pool temperature in selective laser melting," *Prog. Addit. Manuf.*, no. 4, pp. 411-421, 2019.

[32]   H. Yeung, B. M. Lane, M. A. Donmez, J. C. Fox, and J. Neira, "Implementation of Advanced Laser Control Strategies for Powder Bed Fusion Systems," *Procedia Manuf.*, vol. 26, pp. 871–879, 2018.

[33]   T. Craeghs, F. Bechmann, S. Berumen, and J. P. Kruth, "Feedback control of Layerwise Laser Melting using optical sensors," in *Physics Procedia*, vol. 5, no. PART 2, pp. 505-514, 2010.

[34]   P. Mercelis, J. P. Kruth, and J. Van Vaerenbergh, "Feedback control of selective laser melting," *Proc. 15th Int. Symp. Electromachining, ISEM 2007*, pp. 421–426, 2007.

[35]   M. Hirsch *et al.*, "Assessing the capability of in-situ nondestructive analysis during layer based additive manufacture," *Addit. Manuf.*, vol. 13, pp. 135–142, 2017.

[36]   A. G. Demir, C. De Giorgi, and B. Previtali, "Design and Implementation of a Multisensor Coaxial Monitoring System with Correction Strategies for Selective Laser Melting of a Maraging Steel," *J. Manuf. Sci. Eng. Trans. ASME*, vol. 140, no. 4, 2018.

[37]   B. Lane *et al.*, "Measurements of Melt Pool Geometry and Cooling Rates of Individual Laser Traces on IN625 Bare Plates," *Integr. Mater. Manuf. Innov.*, vol. 9, no. 1, pp. 16–30, 2020.

[38]   M. Pacher, L. Mazzoleni, L. Caprio, A. G. Demir, and B. Previtali, "Estimation of melt pool size by complementary use of external illumination and process emission in coaxial monitoring of selective laser melting," *J. Laser Appl.*, vol. 31, no. 2, p. 022305, 2019.

[39]   L. Mazzoleni, L. Caprio, M. Pacher, and A. G. Demir, "External Illumination Strategies for Melt Pool Geometry Monitoring in SLM," *JOM*, 2018.

[40]   M. Adnan, Y. Lu, A. Jones, and F. T. Cheng, "Application of the Fog Computing Paradigm to Additive Manufacturing Process Monitoring and Control," pp. 254–267, 2019.

[41] S. Clijsters, T. Craeghs, S. Buls, K. Kempen, and J.-P. Kruth, "In situ quality control of the selective laser melting process using a high-speed, real-time melt pool monitoring system," *Int. J. Adv. Manuf. Technol.*, vol. 75, no. 5, pp. 1089–1101, 2014.

[42] E. Vasileska, A. G. Demir, B. M. Colosimo, and B. Previtali, "Layer-wise control of selective laser melting by means of inline melt pool area measurements," *J. Laser Appl.*, vol. 32, no. 2, p. 022057, 2020.

[43] P. A. Hooper, "Melt pool temperature and cooling rates in laser powder bed fusion," *Addit. Manuf.*, vol. 22, no. May, pp. 548–559, 2018.

[44] J. C. Heigel and B. M. Lane, "Measurement of the Melt Pool Length during Single Scan Tracks in a Commercial Laser Powder Bed Fusion Process," *J. Manuf. Sci. Eng. Trans. ASME*, vol. 140, no. 5, p. 051012, 2018.

[45] A. B. Spierings and G. Levy, "Comparison of density of stainless steel 316L parts produced with Selective Laser Melting using different powder grades," *20th Annu. Int. Solid Free. Fabr. Symp. SFF*, no. December, pp. 342–353, 2009.

[46] B. Lane, S. Moylan, E. P. Whitenton, and L. Ma, "Thermographic measurements of the commercial laser powder bed fusion process at NIST," *Rapid Prototyp. J.*, vol. 22, no. 5, pp. 778–787, 2016.

[47] S. S. Sih and J. W. Barlow, "The prediction of the emissivity and thermal conductivity of powder beds," *Part. Sci. Technol.*, vol. 22, no. 4, pp. 427–440, 2004.

[48] P. Fischer, V. Romano, H. P. Weber, N. P. Karapatis, E. Boillat, and R. Glardon, "Sintering of commercially pure titanium powder with a Nd:YAG laser source," *Acta Mater.*, vol. 51, no. 6, pp. 1651–1662, 2003.

[49] T. Phillips, T. Ricker, S. Fish, and J. Beaman, "Design of a laser control system with continuously variable power and its application in additive manufacturing," *Addit. Manuf.*, vol. 34, no. November 2019, p. 101173, 2020.

List of tables

List of figures